Li et al. BMC Medicine (2026) 24:255
https://doi.org/10.1186/s12916-026-04785-0

BMC Medicine

RESEARCH

Open Access

Downregulated lysyl oxidase in plasma extracellular vesicles: a biomarker linked to brain metastasis risk in lung adenocarcinoma

Jing Li[1,2†], Yu Pei[1,2†], Jia-Li Sun[2†], Fen Hu[1,2], Han-Xue Yang[1,2], Jun Zhou[1,2], Cong-Ting Wu[2], Xingjie Hao[2], Wei Gong[1,2*], Yang Yao[1,2*] and Yi Liu[3*]

Abstract

Background Brain metastasis (BrM) is a leading cause of mortality in patients with lung adenocarcinoma (LUAD). Extracellular vesicles (EVs), which carry bioactive molecules, play a critical role in tumor microenvironment remodeling and exhibit metastatic organotropism, holding promise as liquid biopsy biomarkers. This study aims to identify plasma EV-derived proteins associated with LUAD-BrM.

Methods A multi-omics framework was applied. Plasma EVs from 59 stage IV LUAD patients (30 BrM vs 29 non-BrM) were profiled using data-independent acquisition mass spectrometry proteomics. Candidate proteins were screened via bioinformatics and machine learning (LASSO/RF/SVM). Initial validation included tissue proteomics ($n=13$), single-cell transcriptomics (TISCH2), and Western blot analysis of a subset of the discovery samples. Functional experiments were conducted in vitro. The lead candidate was ultimately validated in an independent plasma cohort ($n=158$) through ELISA.

Results Proteomic analysis implicated collagen-containing extracellular matrix (ECM) pathways. Lysyl oxidase (LOX), a key ECM cross-linking enzyme, was identified as a lead candidate. LOX and its family member LOXL1 were consistently downregulated in BrM tissues and plasma EVs. Single-cell analysis revealed decreased LOX expression specifically in BrM-associated fibroblasts, which showed suppressed ECM-related pathways. In vitro experiments supported a PI3K/AKT-LOX-ECM regulatory axis. Plasma EV-derived LOX demonstrated strong diagnostic performance in the independent cohort, with an AUC of 0.786 (95% CI 0.713-0.859).

Conclusions Our study establishes plasma EV-derived LOX as a promising non-invasive biomarker for LUAD-BrM through a comprehensive multi-omics validation strategy. We propose a model wherein downregulation of LOX, potentially driven by PI3K/AKT signaling in tumor-associated fibroblasts, contributes to ECM degradation and may promote brain-tropic metastasis. This finding offers new insights for risk stratification and timely intervention in LUAD patients.

†Jing Li, Yu Pei and Jia-Li Sun contributed equally to this work.

*Correspondence:
Wei Gong
Gongwei@hbuas.edu.cn
Yang Yao
tjyaoyang@163.com
Yi Liu
1069@hbucm.edu.cn
Full list of author information is available at the end of the article

Keywords Lung adenocarcinoma, Brain metastasis, Extracellular vesicles, Lysyl oxidase, Liquid biopsy

Background

Lung cancer, the leading cause of cancer-related deaths globally, has the highest incidence among malignancies [1]. Non-small cell lung cancer (NSCLC) constitutes about 85% of cases. Compared with squamous cell carcinoma, lung adenocarcinoma (LUAD) demonstrates a particularly high propensity for brain metastasis (BrM), which occurs in 30–50% of patients [2, 3]. This metastatic tendency may be linked to the distinct driver gene profile and hematogenous spread patterns of LUAD. BrM leads to severe neurological deficits and markedly reduced quality of life, while current treatments remain largely ineffective, often yielding a median overall survival of under 12 months [4]. Although advanced imaging techniques such as high-resolution MRI and PET-CT have improved early detection of asymptomatic BrM, they impose substantial financial burdens and struggle to differentiate true progression from pseudoprogression or radiation necrosis [5, 6]. Therefore, there is an urgent need to identify non-invasive biomarkers for the early identification of LUAD-BrM and clarify their molecular mechanisms, which would facilitate timely intervention and improve patient prognosis.

Given the risks and limitations of neurosurgical biopsy, understanding the dynamic biological mechanisms of brain metastasis remains challenging. Liquid biopsy offers a non-invasive alternative, capturing tumor heterogeneity through repeated sampling of analytes such as circulating tumor cells, nucleic acids, and extracellular vesicles [7, 8]. Despite its utility in other cancers, liquid biopsy for brain metastases remains underdeveloped [5, 9, 10]. Among these targets, extracellular vesicles (EVs) are particularly promising due to their abundance in bodily fluids, rich molecular cargo (proteins, nucleic acids, lipids), and high stability [11–13]. Tumor-derived EVs (TDEVs) have been identified as a crucial component of the tumor secretome, playing a key role in the bidirectional interactions between tumors and host cells [14, 15]. This is no exception in lung cancer, where they remodel the tumor microenvironment by promoting epithelial-mesenchymal transition, proliferation, immunosuppression, angiogenesis, and hematogenous metastasis, thereby facilitating invasion and metastatic spread [16, 17].

Research has demonstrated that cancer cells exploit TDEV-mediated mechanisms to achieve organ-specific microenvironment remodeling by exhibiting selective affinity for particular receptor cells, thereby directing metastatic organotropism and mediating non-random metastatic patterns [18, 19]. Mounting evidence indicates that TDEV-associated proteins and nucleic acids facilitate communication between tumor cells and the brain microenvironment, promoting the establishment of brain metastases [20]. Hoshino et al. revealed that exosomal integrins dictate organ-specific metastasis, with α6β4 and α6β1 associated with lung metastasis and αvβ5 linked to liver metastasis [21]. Their team further identified elevated levels of migration-induced hyaluronan-binding protein in both tumor tissues and EVs from patients with brain metastases, which was not observed in cases of lung or bone metastasis [22]. Advances in proteomics have uncovered molecular features of TDEV-driven organotropic metastasis, highlighting exosomal proteins as encoders of organ-specific metastatic information. Thus, plasma exosomal proteins represent promising non-invasive biomarkers for predicting LUAD-BrM.

In this study, peripheral blood plasma samples from patients diagnosed with stage IV LUAD were categorized based on the presence or absence of brain metastases (BrM). Initially, EVs were isolated using size exclusion chromatography (SEC), and BrM-associated proteins were identified via data-independent acquisition mass spectrometry (DIA-MS) and bioinformatic analysis. Subsequently, candidate proteins were further refined through protein–protein interaction (PPI) network analysis, machine learning algorithms, and proteomic profiling of formalin-fixed paraffin-embedded (FFPE) tissue samples. Finally, validation was performed through the single-cell database, immunohistochemistry (IHC), and diagnostic evaluation via enzyme-linked immunosorbent assay (ELISA). The flow diagram of the study is presented in Fig. 1. With a cohort of 216 patients, this study represents the largest investigation to date of plasma exosomal biomarkers for LUAD-BrM. This research aims to provide a novel liquid biopsy tool for monitoring high-risk populations and establish a foundation for elucidating molecular mechanisms and developing EV-targeted therapies for LUAD-BrM.

Methods

Patients and samples

A total of 260 patients with pathologically confirmed LUAD who were hospitalized in our institution over the past 4 years and diagnosed with TNM stage IV were included. Based on the presence or absence of brain metastasis, the patients were divided into two groups: the experimental group (BrM) and the control group

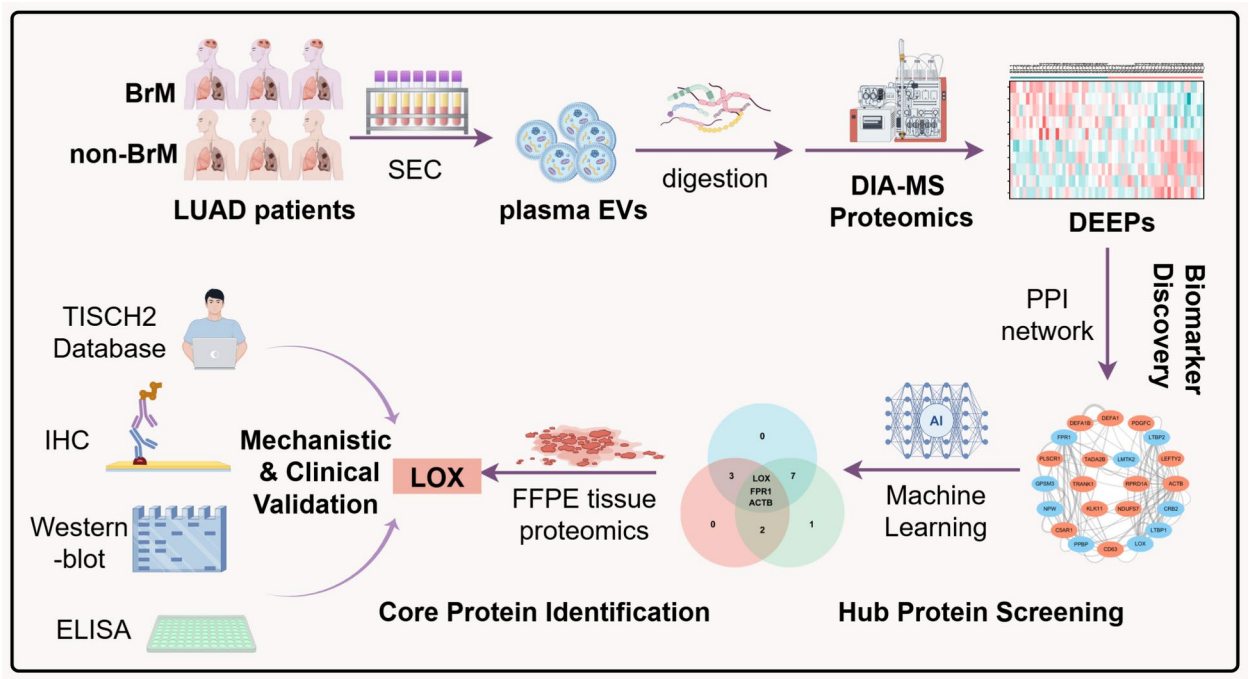

Fig. 1 Flowchart of the study design

(non-BrM). The inclusion criteria for the experimental group required that BrM be first detected by MRI, with no prior brain treatment received. For the control group, inclusion criteria stipulated that no brain metastasis had been detected by MRI before sampling. For proteomic analysis of plasma EVs, the discovery cohort comprised 59 patients (30 BrM and 29 non-BrM), while the validation cohort included 158 patients (79 BrM and 79 non-BrM). For the tissue proteomic study, we included FFPE samples from 5 BrM patients and 8 non-BrM patients, and both groups were derived from the primary lung tumor tissues obtained via biopsy or surgical resection. In the immunohistochemistry experiments, we utilized FFPE samples from 30 patients, which included surgically resected brain tissues from 10 BrM patients, lung puncture biopsy specimens from 10 BrM patients, and lung biopsy specimens from 10 non-BrM patients. The characteristics of all patients are summarized in Additional file 2: Table S1.

For plasma sampling, 5 mL of fasting upper limb venous blood was collected from each participant into EDTA anticoagulant tubes and centrifuged at 4 °C at 3000 × *g* for 10 min. The supernatant plasma layer was carefully aspirated and centrifuged again for 10 min under the same conditions. The supernatant was stored at − 80 °C for subsequent EV extraction. FFPE specimens for proteomic analysis and LOX immunohistochemical staining were obtained from the pathology department of our institution. The specimens were sectioned into 8-μm- and 3-μm-thick slices, respectively.

Isolation and characterization of plasma EV

The collected plasma samples were subjected to EV isolation using size exclusion chromatography (SEC) kits (DL210340, Duolaimi Biotech Co., Ltd.) according to the manufacturer's instructions, utilizing 0.5 ml of plasma per sample. Subsequently, two of the obtained EV samples were randomly selected and characterized through transmission electron microscopy (TEM), nanoparticle tracking analysis (NTA), and Western blotting. A volume of 10 μL of the isolated plasma-derived EVs were deposited onto a copper mesh and negatively stained for 5 min with 2% phosphotungstic acid. The morphology was observed using an HT7700 TEM (Hitachi, Japan). The size distribution and concentration of the EVs were determined after diluting the sample with PBS to an appropriate concentration, employing a ZetaView PMX120 NTA (Particle Metrix, Germany). The detailed procedures for Western blotting are provided in the following section.

Proteomic analysis and bioinformatics analysis

This study employed data-independent acquisition mass spectrometry (DIA-MS) technology, directly constructing a spectral library based on the direct DIA strategy to achieve protein identification and quantification. Before being subjected to LC–MS/MS, EVs underwent a series

of steps, including protein extraction, digestion, and desalting. For specific details regarding sample pretreatment and mass spectrometry instrument conditions, please refer to Additional file 1.

The identified plasma EV-derived proteins were compared with the ExoCarta (http://www.exocarta.org) [23] and Vesiclepedia (http://www.microvesicles.org) [24] databases. Gene Ontology (GO) enrichment analysis and Reactome pathway assessment were conducted using the R "clusterProfiler" package. To refine the data, differentially expressed exosomal proteins (DEEPs) were filtered using the R "limma" package, ensuring that only relevant proteins were included in subsequent analyses. Visual representations of this data were generated through heat mapping and soft clustering techniques, facilitated by the "pheatmap" and "Mfuzz" tools, respectively. Gene Set Enrichment Analysis (GSEA) was performed with the R "clusterProfiler" package. GO enrichment and Kyoto Encyclopedia of Genes and Genomes (KEGG) pathway analyses were conducted using the gseGO and gseKEGG functions, applying thresholds of $P < 0.01$, $|NES| > 1.0$, and FDR $q < 0.05$. Among all the DEEPs, only PPIs with an average scoring greater than 0.7 were included, highlighting the most significant interactions. The CytoHubba plug-in for Cytoscape was employed to identify central hub proteins within these networks. Furthermore, co-expression networking was evaluated using the GeneMANIA database (http://www.genemania.org/), providing a comprehensive understanding of the interactions and relationships among the identified proteins. Following the identification of candidate hub proteins through protein–protein interaction (PPI) network analysis, three distinct machine learning algorithms were employed to refine the selection: Least Absolute Shrinkage and Selection Operator (LASSO) for feature selection, Random Forest (RF) for assessing feature importance, and Support Vector Machine (SVM) for evaluating classification performance.

We analyzed single-cell RNA sequencing (scRNA-seq) data from four independent datasets (GSE143423 [25, 26], GSE150660 [27, 28], GSE127465 [29, 30], and GSE148071 [31, 32]) obtained through the Tumor Immune Single-cell Hub 2 (TISCH2) database (http://tisch.comp-genomics.org) [33], which provides annotated tumor microenvironment profiles across cancer types. Standard preprocessing and cell type annotation were performed utilizing the analytical pipelines and cell label definitions provided by TISCH2. To explore signaling pathways associated with LOX expression, the annotated fibroblasts were further subdivided into LOX-high (LOX-P) and LOX-low (LOX-N) subpopulations based on the median expression level of LOX. Subsequently, Gene Set Variation Analysis (GSVA) was performed using the R package "GSVA" with the 50 Hallmark gene sets [34], and the PROGENy model (using 500 signature genes) [35] was applied to score pathway activity for each subpopulation independently. Pathways significantly enriched (FDR $q < 0.05$) across both datasets were identified for downstream analysis. We investigated the protein expression levels of LOX and LOXL1 in lung adenocarcinoma using the UALCAN database [36].

Immunohistochemistry (IHC)

The expression of LOX, LOXL1, and extracellular matrix-related proteins collagen I and α-smooth muscle actin (α-SMA) was validated through immunohistochemistry (IHC) in formalin-fixed paraffin-embedded (FFPE) tissue sections. Comprehensive experimental procedures, including details on antibodies, staining conditions, and specifications for the kits used, are available in Additional file 1.

Western blot analysis

Protein expression was analyzed by Western blot in three contexts: (a) to characterize isolated plasma EVs, (b) to validate findings in patient-derived samples, and (c) to assess functional changes in vitro.

(a) Characterization of plasma EVs: EV lysates were resolved by SDS-PAGE and electrophoretically transferred onto a polyvinylidene fluoride membrane. After blocking with 5% skim milk, the membrane was probed overnight at 4 °C with the following primary antibodies: anti-CD81 (66,866–1-Ig, Proteintech), anti-CD9 (25,597–1-AP, Proteintech), anti-TSG101 (ab125011, Abcam), anti-HSP70 (10,995–1-AP, Proteintech), and anti-Calnexin (ab22595, Abcam). Subsequently, the membrane was washed and incubated with HRP-conjugated secondary antibodies (SA00001-1 and SA00001-2, Proteintech) for 1 h at room temperature. Protein bands were visualized using an enhanced ECL detection kit (BL520A, Biosharp) and imaged with an Amersham ImageQuant 800 system (Cytiva, USA).

(b) Validation in Patient Tissues and Plasma EVs: To further validate the downregulation of LOX and LOXL1 at the protein level, Western blot analysis was performed on primary lung tumor tissues and plasma EVs. Primary lung tumor tissue samples along with six matched plasma samples (BrM vs. non-BrM, 3 vs. 3) were randomly selected from independent validation cohort including 158 LUAD patients. Tissue samples were obtained via biopsy, immediately snap-frozen in liquid nitrogen, and stored at − 80 °C until use. Plasma EVs were isolated from the corresponding patient plasma using SEC kits as previ-

ously described. For tissue samples, approximately 30 mg of frozen tissue was homogenized in RIPA lysis buffer containing protease inhibitors. Protein concentration was determined using the BCA assay. For plasma EV samples, the SEC-isolated EV fraction was lysed by ultrasonication. Equal amounts of protein (20 μg from tissue lysates or 15 μL of plasma EVs at a concentration of 1.2×10^{10} particles/mL) were separated by SDS-PAGE and transferred to PVDF membranes. The membranes were blocked and incubated overnight at 4 °C with primary antibodies. For tissue samples, the primary antibodies included LOX (Proteintech, 17,958–1-AP, 1:600), LOXL1 (Proteintech, 26,608–1-AP, 1:1000), and GAPDH (Proteintech, 10,494–1-AP, 1:5000) as a loading control. For plasma EV samples, in addition to LOX and LOXL1, we assessed the expression of canonical EV markers (CD9, TSG101, HSP70) and the negative marker Calnexin to confirm EV purity and loading consistency. Subsequent incubation with HRP-conjugated secondary antibodies, chemiluminescent development, and imaging were performed as described.

(c) Functional Validation in Cell Models: To model the tumor-stroma interaction and investigate the PI3K/AKT-LOX-ECM axis, human lung adenocarcinoma cells (A549) were cultured to 70–80% confluence. The conditioned medium (CM) was collected, centrifuged to remove cell debris, and stored at − 80 °C. Human lung fibroblasts (MRC-5) were then treated with a 1:1 mixture of A549-CM and fresh medium for 24 h to simulate the tumor microenvironment. For pathway inhibition studies, cells were subsequently treated with either the PI3K inhibitor PI3K-IN-1 (25 μM, HY-12068, MedChemExpress) or the LOX inhibitor LOX-IN-3 (1 μM, HY-138625, MedChemExpress) for an additional 48 h. DMSO was used as the vehicle control. After treatment, cells were harvested and lysed. Western blot was then performed as described previously, using antibodies against LOX (Proteintech, 17,958–1-AP, 1:1000), phospho-AKT (Cell Signaling Technology, 4060S, 1:2000), total AKT (Cell Signaling Technology, 4691S, 1:2000), Collagen I (Abcam, ab34710, 1:1000), α-SMA (Cell Signaling Technology, 19245S, 1:1000), and GAPDH (Proteintech, 10,494–1-AP, 1:5000). All the experiments were performed with at least three independent biological replicates.

Enzyme-linked immunosorbent assay (ELISA)

The plasma samples from 158 patients in the validation cohort underwent EV extraction and treatment with an EV-specific lysis solution, as previously described. Following this, the supernatant was collected after centrifugation at $14{,}000\times g$ for 20 min. Prior to enzyme-linked immunosorbent assay (ELISA) detection, the protein concentrations of the samples were standardized to similar levels using the BCA assay. The expression levels of LOX in both groups were measured using the Human LOX ELISA Kit (HM10997, Bioswamp), in accordance with the manufacturer's instructions. Additionally, the concentrations of LOX in the plasma samples were determined for comparison.

Statistical analysis

Binary logistic regression was conducted on the data using IBM SPSS Statistics software (version 23.0) prior to plotting the Receiver Operating Characteristic (ROC) curve for the combined biomarkers. All other statistical analyses and graph preparations were performed using GraphPad Prism software (version 10.4.2) or the R package (version 4.3.1). Differences between groups were analyzed using the Mann–Whitney *U* test or the Kruskal–Wallis test, with statistical significance set at $P<0.05$.

Results

Characterization of the plasma EVs

The plasma-derived EVs obtained from two randomly selected samples were characterized through transmission electron microscopy (TEM), nanoparticle tracking analysis (NTA), and Western blotting successively. TEM images revealed that both samples exhibited the typical cup-shaped morphology characteristic of EVs (Fig. 2A,B). NTA indicated that their sizes predominantly ranged from 40 to 130 nm (Fig. 2C). Western blotting experiments provided immunoblotting band images of exosomal proteins, as illustrated in Fig. 2D. Notably, CD9, CD81, and TSG101 were detected in the EVs, while Calnexin, utilized as a negative control, was absent. These results indicate that the plasma EVs isolated through SEC were accurately identified.

Proteomic profiling analysis of plasma EVs

Proteomic data obtained from LC–MS/MS were processed with *k*-nearest neighbor imputation and $\log_2$ transformation, followed by quantile normalization to minimize technical variation. Box plots confirmed consistent median expression after normalization (Additional file 1: Fig. S1A–B). All normalized protein values are presented in Additional file 2: Table S2. Partial least squares discrimination analysis (PLS-DA) revealed clear separation between groups (Additional file 1: Fig. S1C), with high intra-group consistency (Additional file 1: Fig. S1D), thereby supporting appropriate sample grouping and high data quality.

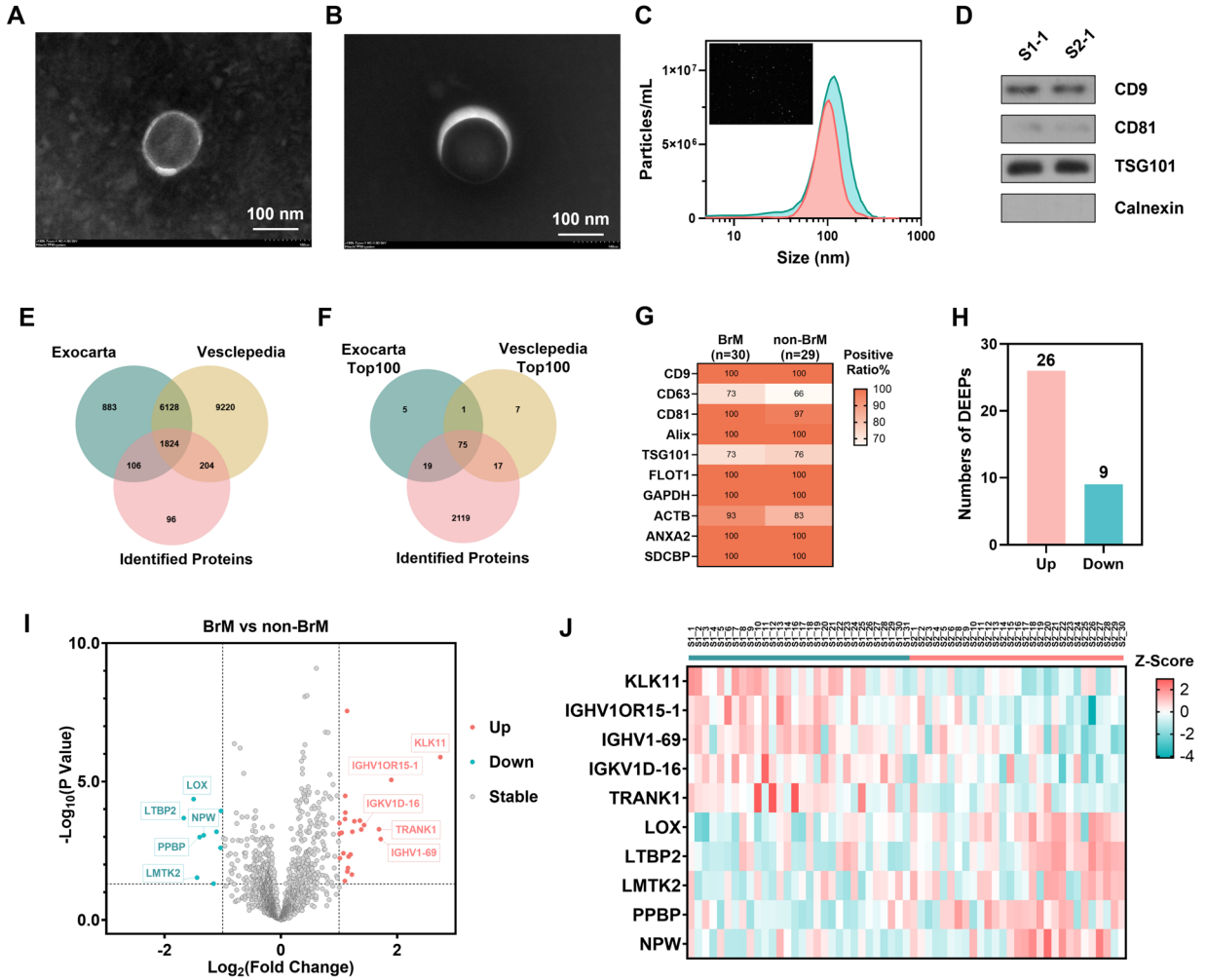

Fig. 2 Characterization of plasma-derived EVs obtained from two randomly selected samples and proteomic analysis of plasma-EVs from the discovery cohort (BrM vs non-BrM, 30 vs 29). **A,B** TEM images. **C** Particle distribution. **D** Immunoblotting band images of exosomal proteins. **E** Venn diagram of the identified proteins compared with the proteins within Exocarta and Vesiclepedia databases. **F** venn diagram of the identified proteins compared with the TOP 100 proteins within Exocarta and Vesiclepedia databases. **G** Positive expression rates of the top 10 proteins from both databases across the two groups. **H** Numbers of DEEPs in BrM group compared to non-BrM group. **I** Volcano plot. **J** Heatmap illustrating the expression patterns of the top upregulated and downregulated exosomal proteins associated with LUAD-BrM after *Z*-score standardization

A total of 2230 proteins were identified in plasma EVs from the 59-patient discovery cohort. GO enrichment analysis indicated strong association with secretory and cytoplasmic vesicle lumens and blood particles (Additional file 1: Fig. S2A), thus confirming both the purity of the EVs and their plasma origin. Over 80% of the identified proteins overlapped with the Exocarta and Vesiclepedia databases (Fig. 2E), with more than 90% of the top 100 proteins from each database being detected (Fig. 2F). The positive expression rates of the top 10 exosomal markers approached 100% in both groups (Fig. 2G), except for CD63 and TSG101, which aligns with findings from a prior study [37]. Collectively, these results underscore the high purity of EVs isolated through SEC.

Among the 2230 identified proteins, 2146 (96.2%) were shared between the two groups, while 58 and 26 proteins were unique to the non-BrM and BrM groups, respectively. Utilizing a threshold of $|\log_2$ Fold Change$|$ Utilizin$P < 0.05$, we identified 35 significantly differentially expressed exosomal proteins (DEEPs): 26 upregulated and 9 downregulated in the BrM group (Fig. 2H and Additional file 2: Table S3). The corresponding volcano plot is presented in Fig. 2I. A heatmap (Fig. 2J) illustrates the expression patterns of the top five upregulated

and downregulated proteins in both groups after *Z*-score standardization. Notably, the expression levels of CD9, Alix, and FLOT1 did not exhibit significant differences between the two groups (Additional file 1: Fig. S2B), indicating that these changes were not attributable to the quantity or composition of the isolated EVs.

Bioinformatics analyses of plasma EVs proteomic profiles and the screen of hub DEEPs

To elucidate the functional implications of the differentially expressed exosomal proteins (DEEPs), we conducted GO and Reactome pathway enrichment analyses. The significantly enriched GO terms across biological process (BP), cellular component (CC), and molecular function (MF) categories are presented in Fig. 3A. The BP terms primarily pertained to immune and chemotactic regulation. Enriched CC terms included immunoglobulin complexes and collagen-containing extracellular matrix (ECM), while antigen binding emerged as the predominant MF term. Reactome analysis underscored pathways associated with ECM organization, such as elastic fiber formation (R-HSA-1566948) and related molecules (R-HSA-2129379) (Fig. 3B).

Given the limited number of DEEPs, we applied GSEA to the full proteome to detect subtle pathway-level alterations. The top enriched GO terms, based on *q*-value, are shown in Fig. 3C. Upregulated processes were associated with chromatin remodeling, whereas downregulated functions encompassed ECM collagen degradation, secretory granule release, and calcium ion binding. Notably, the term related to the collagen-containing ECM (GO:0062023) was significantly suppressed (NES = −1.92, $q < 0.001$) in BrM-derived EVs (Fig. 3D), suggesting the exosomal transport of collagen-degrading enzymes or ECM-remodeling signals that may facilitate blood–brain barrier disruption. These results show strong similarity with previous reports demonstrating downregulation of ECM receptor-interaction pathways in lung tissues derived from the BrM group [38], and are also consistent with the downregulation of related

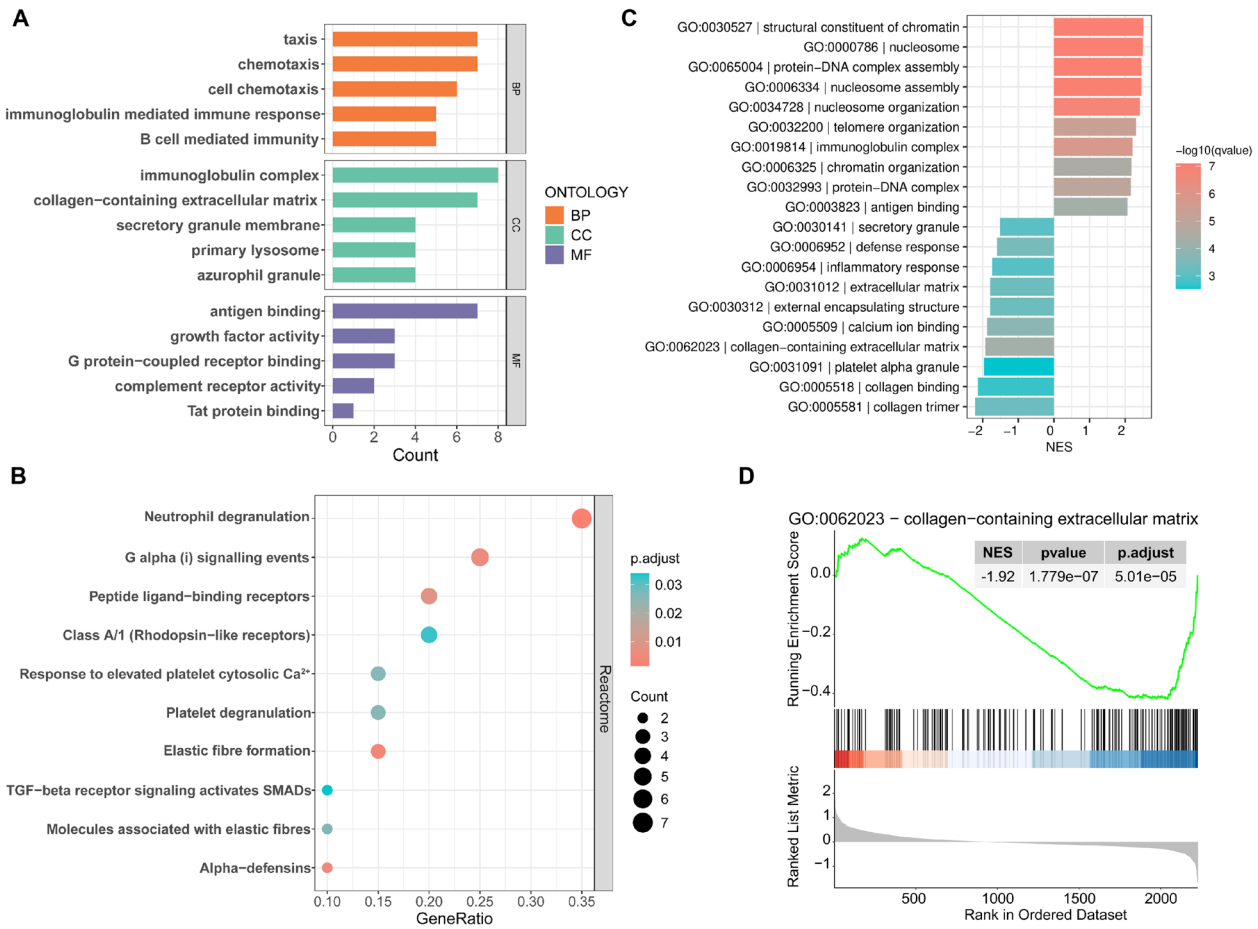

Fig. 3 Functional and pathway enrichment landscape of DEEPs. **A** GO enrichment of DEEPs. **B** Reactome pathway enrichment of DEEPs. **C** GSEA: Enriched GO terms. **D** GSEA enrichment plot: Collagen-containing extracellular matrix

pathways reported by Li et al. in plasma EV proteomics of NSCLC-BrM [37]. Moreover, additional GSEA curves are provided in Additional file 1: Fig. S2(C–F). KEGG analysis revealed a significant downregulation of the complement and coagulation cascades in the BrM group (Additional file 1: Fig. S2G), which are also found in both of these pioneering works [37, 38]. The inhibition of coagulation may alleviate vascular obstruction, thereby sustaining metastatic perfusion while concurrently reflecting ECM degradation, consistent with the suppression of collagen pathways. Collectively, these effects facilitate the detachment of metastatic cells from the vasculature, supporting the notion that EV-mediated ECM degradation may underlie LUAD-BrM.

A PPI network was constructed from the DEEPs using the STRING database (version 12.0). Initially, Cytoscape identified 22 interacting nodes (Fig. 4A), with upregulated and downregulated proteins marked

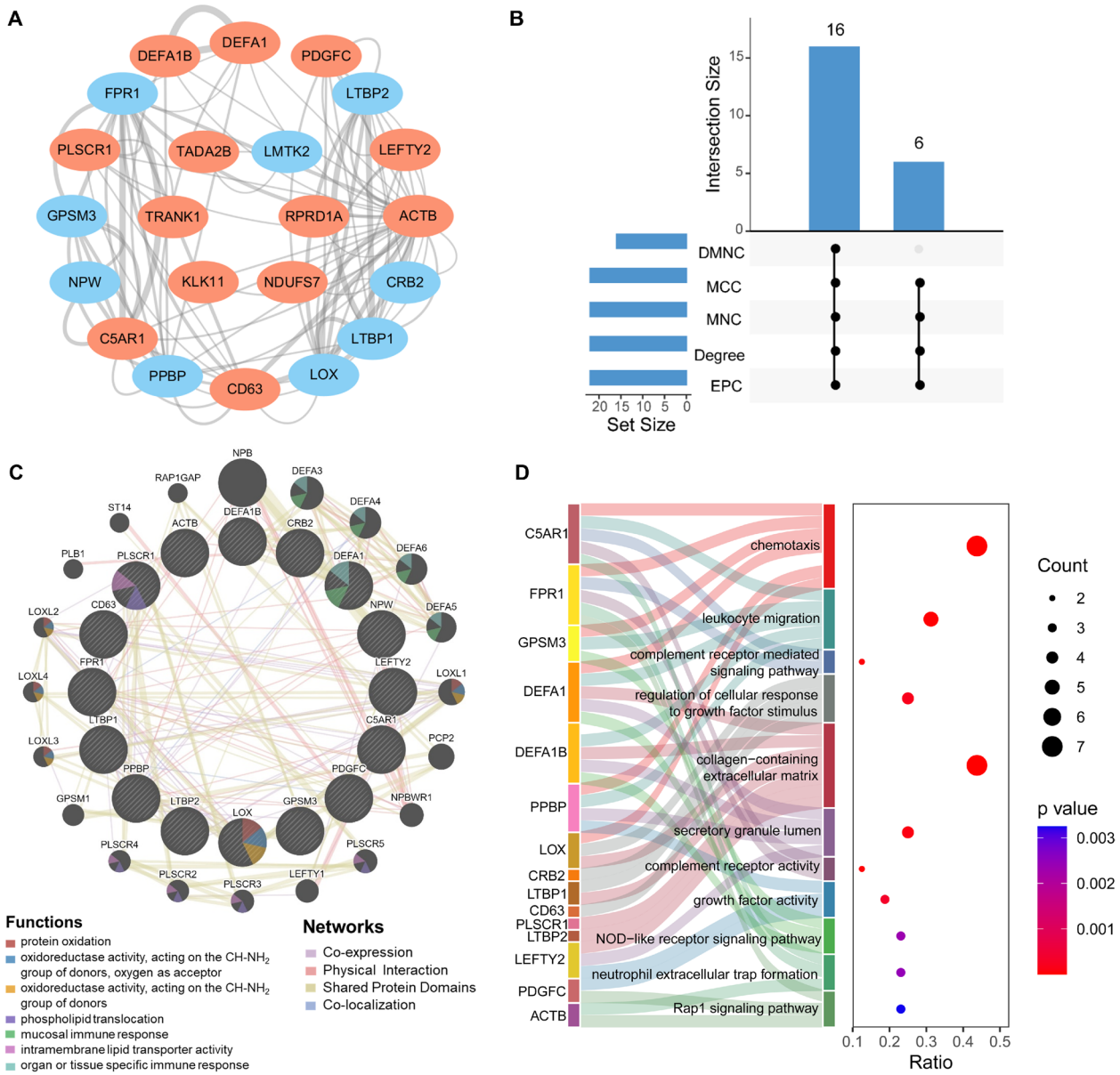

Fig. 4 PPI analysis of the DEEPs associated with LUAD-BrM. **A** PPI network of the DEEPs constructed using the STRING database. **B** Identification of hub proteins from the candidate pool using five distinct network topology algorithms. **C** Functional association network expanded from the 16 hub proteins generated by the GeneMANIA database. **D** Integrated Sankey-bubble plot visualizing the correspondence between the 16 hub proteins and their significantly enriched GO terms/KEGG pathways

in red and blue, respectively. Subsequently, hub protein analysis using five topology algorithms (DMNC, MCC, MNC, Degree, EPC) yielded 16 common candidates: LOX, NPW, PLSCR1, C5AR1, FPR1, GPSM3, DEFA1, DEFA1B, PPBP, CRB2, LTBP2, LTBP1, CD63, PDGFC, LEFTY2, and ACTB (Fig. 4B). To explore the functional associations of these hub proteins, we expanded the network based on the aforementioned 16 hub proteins using the GeneMANIA database (version 3.6.0) (Fig. 4C). The results indicated that their interactions were primarily composed of co-expression (55.26%), physical interactions (18.22%), domain sharing (23.32%), and co-localization (3.20%). Finally, we conducted GO functional annotation and KEGG pathway enrichment analysis for these 16 hub proteins, integrating and visualizing the enrichment results using a Sankey bubble diagram (Fig. 4D). The analysis revealed that most hub proteins were significantly enriched in the term of the collagen-containing extracellular matrix, further confirming their potential role in driving the occurrence of LUAD-BrM through ECM-related mechanisms.

To refine the selection of hub proteins, we employed three machine learning algorithms: LASSO, RF, and SVM. LASSO regression effectively reduced redundant variables through L1 regularization, identifying 13 key proteins with the strongest biological interpretability: ACTB, C5AR1, CD63, DEFA1, DEFA1B, FPR1, GPSM3, LEFTY2, LOX, NPW, PDGFC, PLSCR1, and PPBP (Fig. 5A). RF evaluated feature contributions based on the Mean Decrease Gini Index, retaining eight high-impact proteins with Gini values exceeding 1.5: ACTB, PLSCR1, PDGFC, FPR1, PPBP, LOX, LTBP2, and LTBP1 (Fig. 5B). SVM Recursive Feature Elimination (SVM-RFE) optimized the hyperplane by maximizing the classification margin, identifying 14 proteins with the highest classification discriminative power: ACTB, C5AR1, CD63,

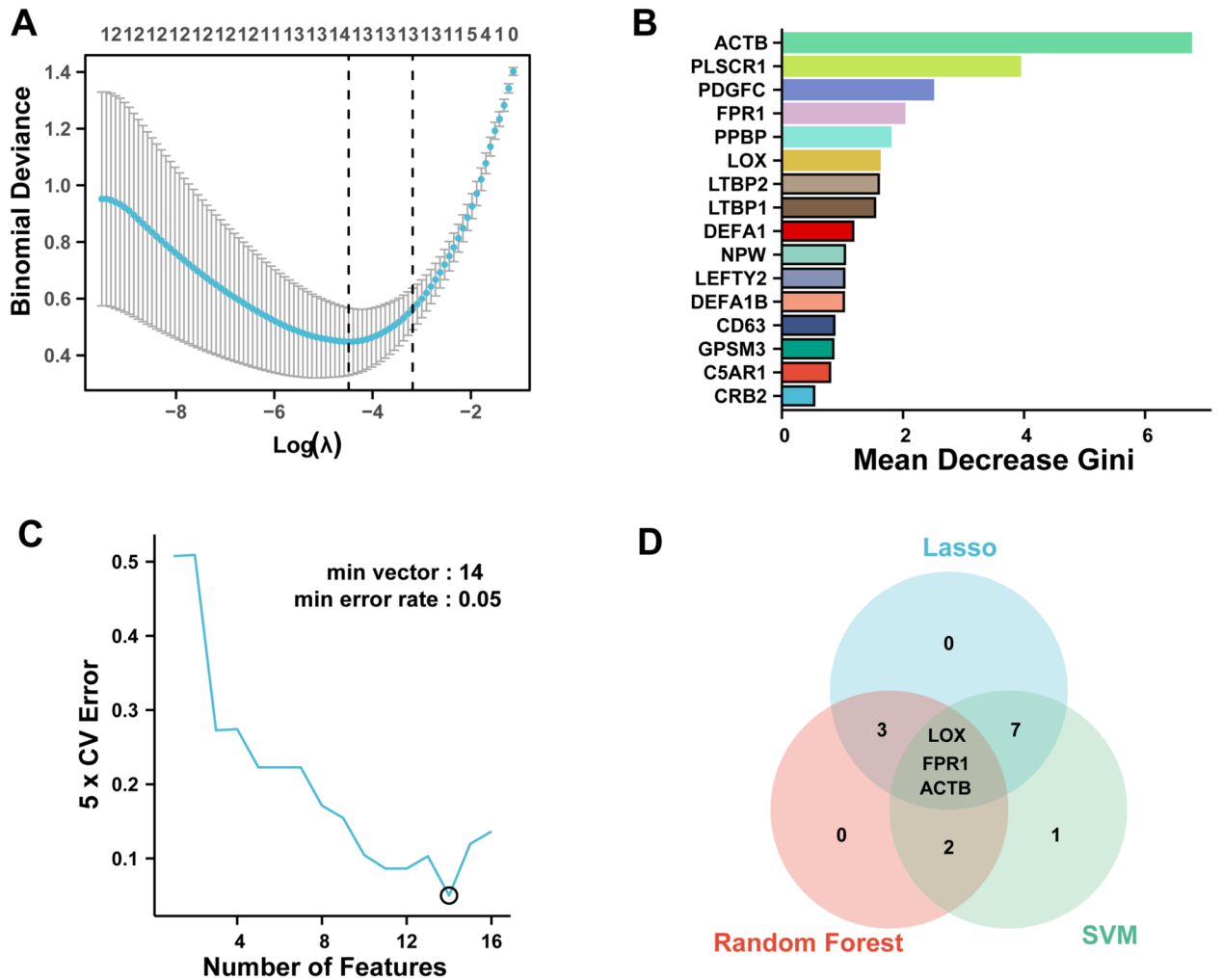

Fig. 5 Enhanced screening of candidate proteins through three machine learning algorithms. **A** LASSO regression coefficient analysis. **B** RF feature importance. **C** SVM -RFE feature selection with fivefold cross-validation. **D** Venn diagram of the hub proteins screened by the three algorithms

CRB2, DEFA1, DEFA1B, FPR1, GPSM3, LEFTY2, LOX, LTBP1, LTBP2, NPW, and PDGFC (Fig. 5C). The intersection of the three methods revealed three consensus candidates: LOX, FPR1, and ACTB (Fig. 5D), indicating their robust association with LUAD-BrM across different modeling approaches.

Integrated analysis of small-cohort FFPE tissue proteomics

We conducted a proteomics analysis on FFPE primary lung tumor tissue samples from a small cohort of LUAD patients, comprising 5 patients with BrM and 8 patients with metastases to other sites. Figure 6A and B present the cluster heatmap and volcano plot of differentially expressed proteins (DEPs), respectively. Utilizing the screening criteria of $|\log_2\text{Fold Change}| > 1$ and $P < 0.05$, we identified 191 significantly upregulated proteins and 363 downregulated proteins (Fig. 6C and Additional file 2: Table S4). When comparing this protein set with the three LUAD-BrM-associated EV-derived hub proteins identified in previous screenings, formyl peptide receptor 1 (FPR1) emerged as the only overlapping protein (Fig. 6D). However, FPR1 displayed an opposing expression trend in brain metastasis samples; it was downregulated in plasma EVs but upregulated in tissue (Fig. 6E). This contradiction suggests a potential influence from sample heterogeneity, leading us to refrain from further exploring FPR1 as a target. Notably, Lysyl oxidase-Like 1 (LOXL1) was significantly downregulated in brain metastasis tissue ($\text{Log}_2\text{Fold Change} = -1.43$, $P = 0.005$), which is consistent with the downregulation of LOX in plasma EVs (Fig. 6F). LOXL1 and LOX are both members of the lysyl oxidase family, catalyzing the oxidation and deamination of lysine residues in collagen and elastin to enhance ECM mechanical stability [39]. The two proteins share domains within the PPI network in the proteomic analysis of plasma EVs (Fig. 4C), and PPI analysis combining omics data of FFPE tissues and plasma EVs further confirmed the direct interaction between LOX and LOXL1 (Fig. 6G). Additionally, analysis of transcriptomic data from The Cancer Genome Atlas (TCGA) revealed a positive correlation between LOXL1 and LOX mRNA expression ($R = 0.43$, $P < 0.001$; Fig. 6H). Finally, we assessed the expression of LOX, LOXL1, and ECM-related proteins (collagen I and α-SMA) in three sample groups (brain tissue of LUAD-BrM vs. lung tissue of LUAD-BrM vs. lung tissue of LUAD-non-BrM, 10 vs. 10 vs. 10) via immunohistochemistry experiments. As shown in Fig. 6I–J, all these markers were significantly downregulated in the primary lung tumors of LUAD patients with BrM compared to those without BrM. Due to ethical considerations and limited sample availability, normal brain tissue from patients without BrM was not accessible for comparison. Nevertheless, we observed similarly low expression levels of these markers in the available brain metastatic lesions.

To investigate whether the downregulation of the LOX family is specific to the brain metastatic phenotype, we systematically analyzed the expression of LOX and LOXL1 in LUAD tissues compared to normal tissues, as well as across different tumor stages, using two independent cohorts from the UALCAN database. As shown in Additional file 1: Fig. S3, in the first cohort [40, 41] comprising normal lung tissues and LUAD tumors across stages (A, C), LOX expression showed only a marginal upregulation in Stage 3 tumors, with no significant difference in other stages compared to normal tissue, while LOXL1 expression did not show significant alterations at any stage. In the second cohort [42, 43], which included only Stage 1–3 LUAD tumor tissues (B, D), LOX expression did not differ significantly across the three stages; LOXL1 showed a slight downregulation only in Stage 2, returning to a level comparable to Stage 1 by Stage 3. In summary, during the progression of LUAD from normal tissue to primary tumors across stages, LOX and LOXL1 did not exhibit a consistent, stage-dependent downregulation trend. This analysis suggests that the significant downregulation of LOX/LOXL1 observed in our brain metastasis cohort may reflect a potential association with the brain-metastatic phenotype, rather than being solely attributable to overall tumor progression. Combined with the observed cross-dimensional consistency between LOXL1 downregulation in tissues and LOX downregulation in plasma EVs, these findings further indicate that the LOX family may specifically facilitate

(See figure on next page.)

Fig. 6 Integrated analysis of FFPE tissue proteomics and validation of LOX family downregulation in LUAD-BrM. **A** Cluster heatmap and **B** volcano plot of differentially expressed proteins (DEPs) identified in FFPE tissues (BrM vs non-BrM, 5 vs 8). **C** Bar plot showing the number of DEPs. **D** Venn diagram illustrating the overlap between DEPs from FFPE tissue proteomics and the three hub proteins in plasma EV proteomics. **E** Expression of FPR1 in FFPE tissues and plasma EVs (statistical significance determined by the two-sided Mann–Whitney *U* test). **F** Expression of LOXL1 in FFPE tissue and LOX in plasma EVs (statistical significance determined by the two-sided Mann–Whitney *U* test). **G** PPI network between LOXL1 and LOX based on integrated multi-omics data. **H** correlation analysis of LOXL1 and LOX expression levels based on data from TCGA. **I** Representative IHC staining images of LOX, LOXL1, Collagen I, and α-SMA in three tissue groups (Scale bars: 100 μm). **J** Quantitative analysis of IHC staining intensity for LOX, LOXL1, Collagen I, and α-SMA in three FFPE tissue groups ($n = 10$ per group). Data are presented as mean ± SD. Statistical significance between the BrM-lung and non-BrM-lung groups was assessed by the Kruskal–Wallis test, followed by Dunn's post hoc test

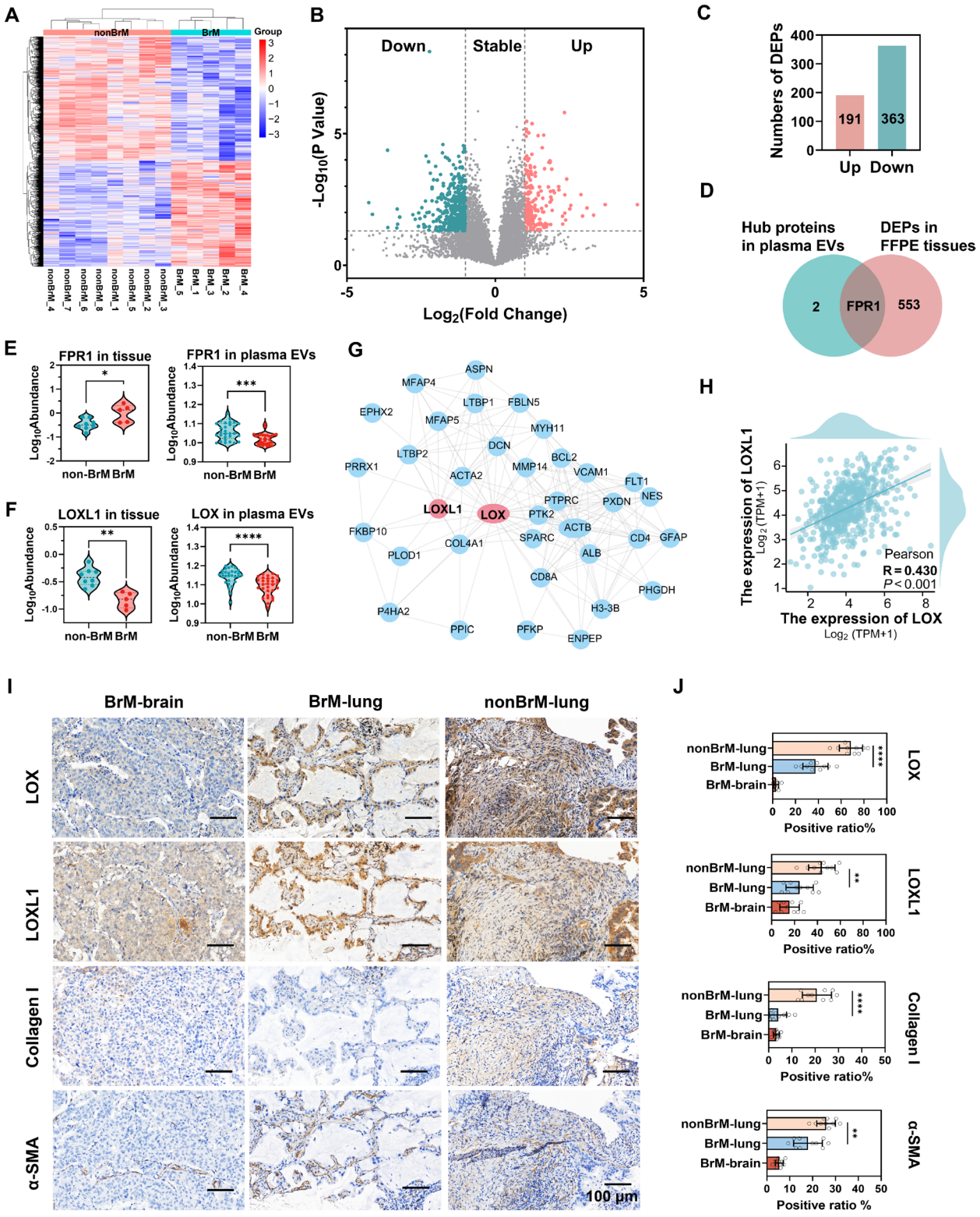

Fig. 6 (See legend on previous page.)

brain metastasis and colonization in LUAD by jointly disrupting ECM homeostasis. Compared to traditional tissue biopsy, LOX in plasma EVs represents a more suitable non-invasive liquid biopsy target for early warning and efficacy monitoring, thereby offering novel strategies for the clinical management of LUAD-BrM.

Single-cell dissection and mechanistic elucidation of LOX in LUAD-BrM

To explore the biological plausibility of plasma EV-derived LOX as a non-invasive marker associated with LUAD-BrM, we investigated its expression pattern at the single-cell transcriptomic level. Initially, we screened four NSCLC datasets from the TISCH2 database, which included two BrM groups (GSE143423, GSE150660) and two in situ groups (GSE127465, GSE148071). Cell type annotation was strictly based on the metadata provided by TISCH2 and previously published subpopulation marker genes. Our analysis revealed that LOX was significantly downregulated in the BrM group (Fig. 7A). In contrast, the NSCLC in situ datasets exhibited markedly higher LOX expression compared to the NSCLC-BrM group, with expression primarily localized to fibroblasts (Fig. 7B). Consequently, fibroblasts in the NSCLC in situ group were further categorized into LOX-high and LOX-low groups based on the median LOX expression level. Differentially expressed genes were identified using the FindAllMarkers function, followed by GO enrichment analysis. As illustrated in Fig. 7C, differentially expressed genes in both in situ datasets were significantly enriched in pathways related to ECM assembly and remodeling, including collagen fibril organization, collagen-containing ECM, ECM structural constituent, and ECM binding function. This transcriptomic evidence is consistent with the downregulation mechanism of ECM-related pathways observed in the proteome of plasma EVs, supporting the biological relevance of LOX in LUAD-BrM.

To elucidate the potential regulatory mechanism underlying LOX downregulation, we integrated computational and experimental approaches. First, single-cell transcriptomic analysis of tumor-associated fibroblasts from NSCLC datasets revealed that LOX-low subpopulations were specifically enriched for the PI3K/AKT signaling pathway as displayed in Fig. 8A–D, suggesting a potential regulatory link. Secondly, we functionally validated this link using an in vitro tumor microenvironment model. Treating lung fibroblasts (MRC-5) with conditioned medium from A549 cells (A549-CM) induced a downregulation of LOX. Importantly, concomitant treatment with the PI3K inhibitor PI3K-IN-1 significantly restored LOX protein levels while effectively suppressing AKT phosphorylation (Fig. 8E), establishing PI3K/AKT activation as an upstream suppressor of LOX expression. Finally, to determine the downstream consequence of LOX loss, we inhibited LOX activity directly in the A549-CM primed fibroblasts. Treatment with the LOX inhibitor LOX-IN-3 not only further reduced LOX levels but also led to a significant decrease in the expression of key ECM components, including Collagen I and the activated fibroblast marker α-SMA (Fig. 8F). This in vitro functional discovery aligns with our observations in patient-derived primary lung tumor tissues, where IHC staining revealed significant reductions in LOX, LOXL1, Collagen I, and α-SMA in the BrM group (Fig. 6I,J).

Collectively, these parallel lines of evidence from patient tissues to in vitro models outline a coherent PI3K/AKT–LOX–ECM regulatory axis, wherein activation of the PI3K/AKT pathway suppresses LOX expression, and the resultant LOX deficiency contributes directly to ECM degradation and fibroblast dysfunction in the brain metastatic microenvironment.

Validation of LOX expression via ELISA and Western blot

We utilized ELISA to assess the expression levels of LOX in plasma EVs and total plasma samples from an independent validation cohort comprising 158 patients with LUAD (BrM vs non-BrM, 79 vs 79). The results indicated that LOX expression was significantly downregulated in both plasma EVs and total plasma from the BrM group (Fig. 9A,B). To further validate the capability of LOX expression levels in plasma EVs and total plasma samples to distinguish patients with LUAD-BrM, we plotted receiver operating characteristic (ROC) curves (Fig. 9C). The area under the curve (AUC) values for LOX in plasma EVs and total plasma samples were 0.786 (95% CI 0.713–0.859) and 0.665 (95% CI 0.579–0.750), respectively, indicating that the detection of LOX in plasma EVs provides superior performance and higher potential for identifying LUAD-BrM compared to direct detection in plasma (Delong test $P=0.035$). When both plasma EV-derived LOX and total plasma LOX were incorporated into the model, the AUC value increased to 0.798 (95% CI 0.729–0.866). However, the inclusion of total plasma LOX resulted in only a marginal increase in AUC ($\Delta AUC=0.012$), with a Delong test p-value of 0.561, suggesting no significant difference in discriminatory power between the two models. Therefore, in the context of optimizing clinical application, employing LOX in plasma EVs as a single biomarker associated with LUAD-BrM presents greater practicality and cost-effectiveness.

To directly validate our proteomic findings at the protein level, we performed Western blot analysis on six randomly selected matched primary lung tissues and plasma EVs (BrM vs non-BrM, 3 vs 3) from the abovementioned independent cohort. Consistent with the proteomic and IHC results, both LOX and

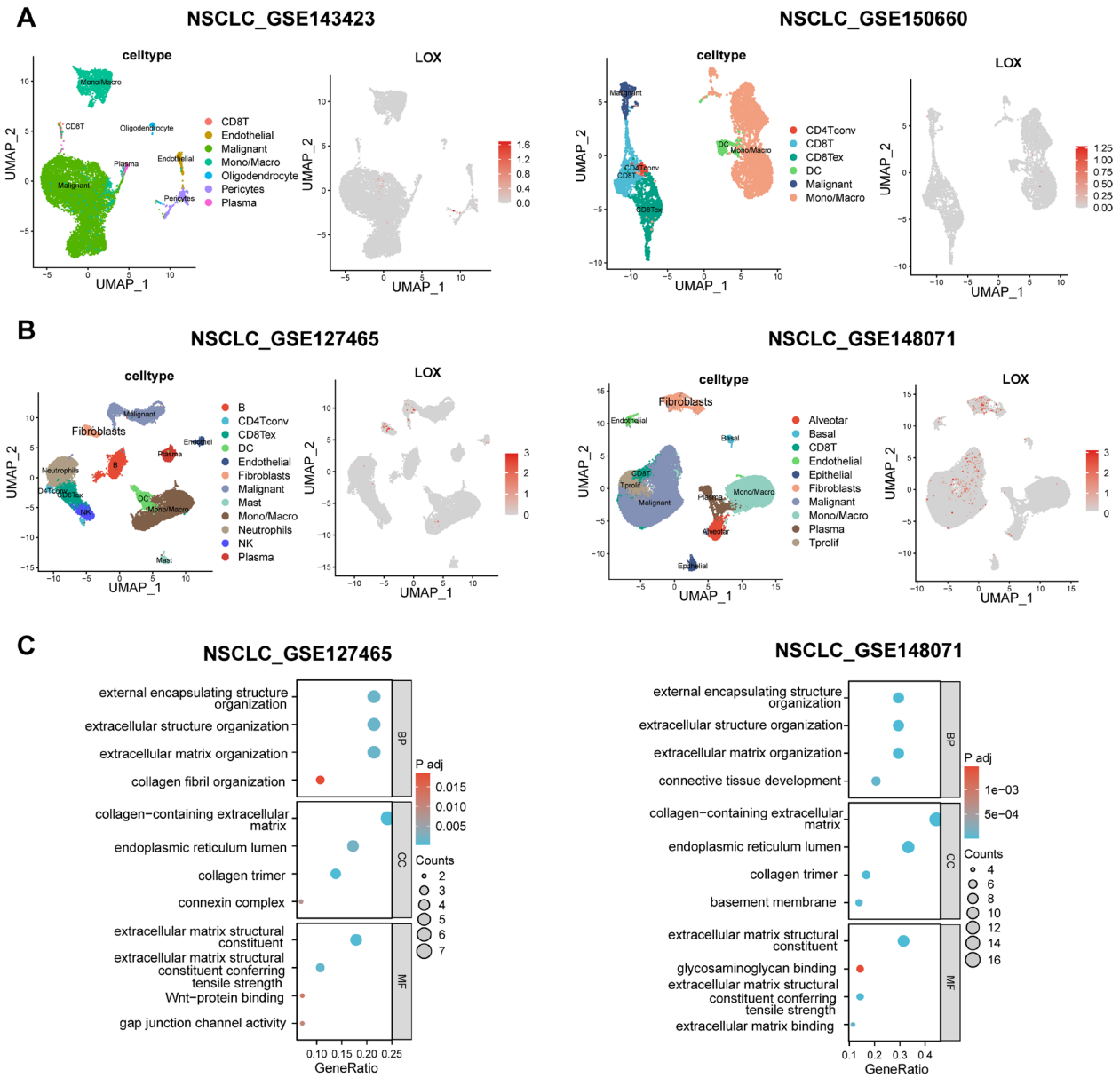

Fig. 7 Single-cell transcriptomic profiling of LOX in NSCLC and its association with ECM pathways. **A,B** Cellular distribution of LOX expression, with predominant fibroblast localization in representative BrM (GSE143423 and GSE150660) and in situ (GSE127465 and GSE148071) datasets. **C** GO enrichment analysis of ECM assembly and remodeling pathways in LOX_HIGH versus LOX_LOW fibroblasts from two NSCLC-in situ datasets

LOXL1 protein levels were substantially decreased in primary lung tumor tissues (Fig. 9D, normalized to GAPDH) and plasma EVs (Fig. 9E) derived from BrM patients compared to non-BrM controls. The purity of plasma EVs was confirmed by the presence of canonical markers (CD9, TSG101, HSP70) and absence of the negative marker Calnexin (Fig. 9E). While this experiment serves as confirmatory protein-level evidence, the primary quantitative and clinically translatable assessment of circulating LOX was conducted via ELISA, which is better suited for standardized liquid biopsy applications.

Discussion

Brain metastasis severely impairs neurological function and quality of life in LUAD patients, underscoring the urgent need for improved prevention, monitoring, and intervention strategies [9]. Despite the application of multi-omics technologies in exploring predictive biomarkers for LUAD-BrM [3, 44–47], the

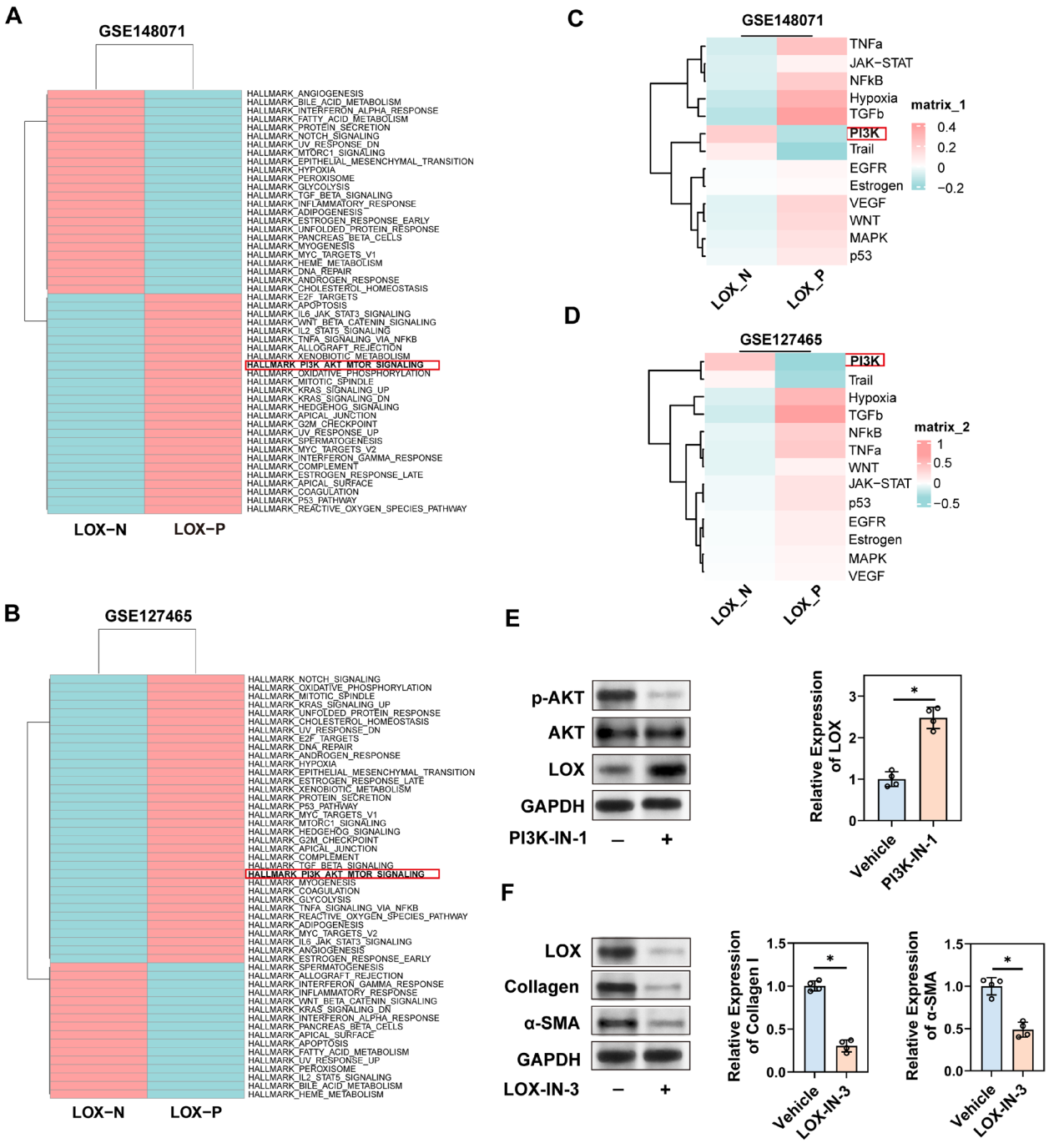

Fig. 8 Functional validation of the PI3K/AKT-LOX-ECM regulatory axis in lung fibroblasts. **A–D** Enrichment of PI3K/AKT signaling pathway activity in LOX-low versus LOX-high fibroblasts from scRNA-seq data. **E,F** Functional analyses identify PI3K as an upstream suppressor of LOX and LOX as a regulator of ECM expression in MRC-5 cells (**E**: Treatment with the PI3K inhibitor PI3K-IN-1 restored LOX expression; **F**: Treatment with the LOX inhibitor LOX-IN-3 reduced the expression of key ECM components). Quantitative analysis of protein levels normalized to GAPDH, with data presented as mean ± SD ($n = 4$ independent experiments). Statistical significance was determined by the two-sided Mann–Whitney *U* test

potential of plasma exosomal proteomics remains largely unexploited. EVs facilitate intercellular communication by transferring bioactive molecules [11, 14], which influence organotropic metastasis and reflect changes in the tumor microenvironment [15, 18–21]. This characteristic renders EV-based liquid biopsy as a minimally invasive alternative for LUAD-BrM compared to traditional tissue biopsies and imaging techniques [6]. Previous studies

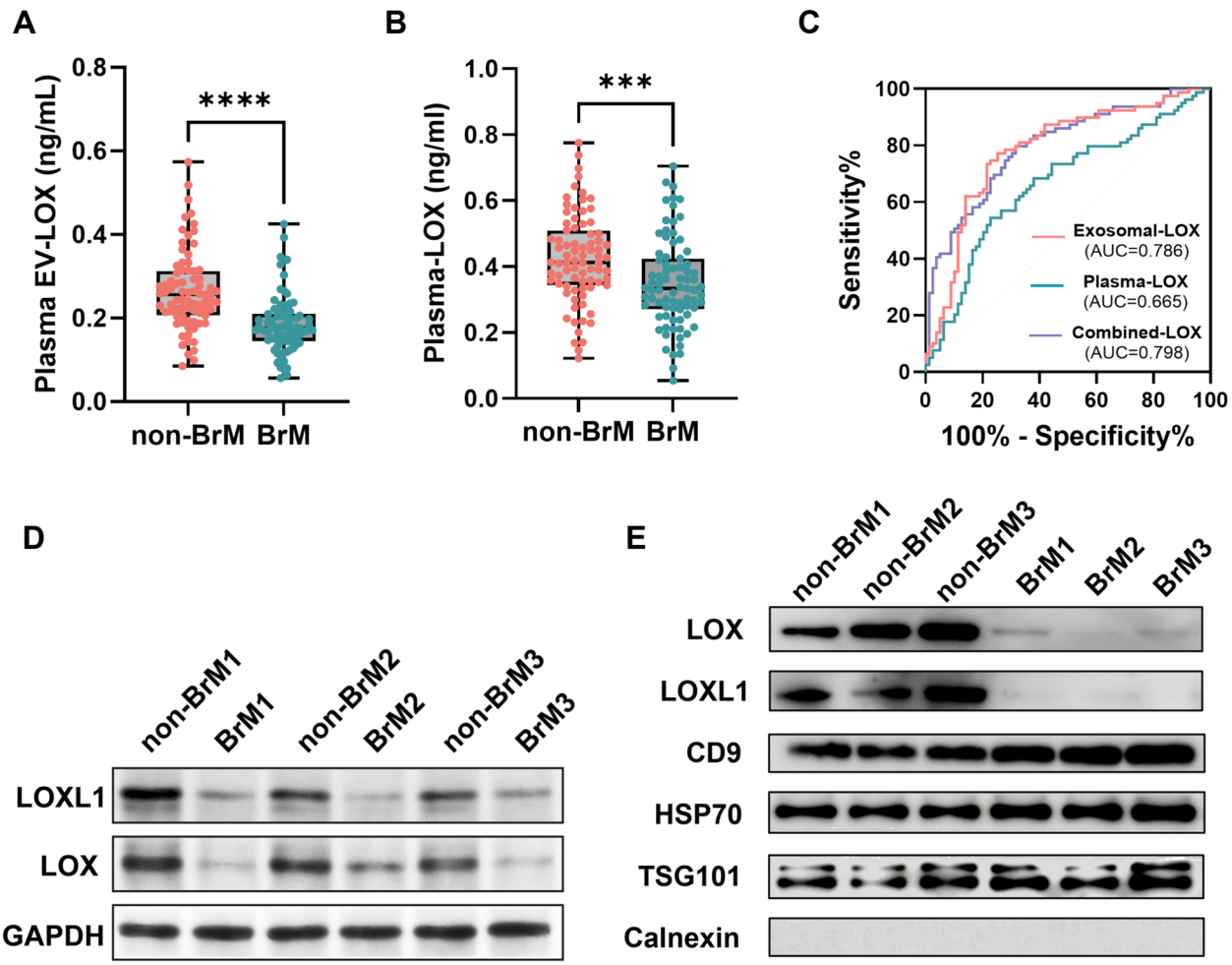

Fig. 9 Validation of LOX downregulation and its diagnostic performance as a plasma EV biomarker for LUAD-BrM. **A,B** Expression levels of LOX in plasma EVs and total plasma from an independent validation cohort (BrM vs non-BrM, 79 vs 79) (**A**: two-sided Mann–Whitney *U* test; **B**: passed the Shapiro–Wilk normality test and following by unpaired two-sided Student's *t* test). **C** Receiver operating characteristic (ROC) curves and area under the curve (AUC) values for discriminating LUAD-BrM based on plasma EV-derived LOX, total plasma LOX, and a combined model. **D,E** Western blot validation of LOX and LOXL1 protein downregulation in **D** matched primary lung tumor tissues and **E** plasma EVs from six randomly selected patients (BrM vs non-BrM, 3 vs 3) of the independent validation cohort

have reported exosomal biomarkers for brain metastasis in small cell lung cancer and NSCLC [37, 48]. However, despite LUAD being the lung cancer subtype with the highest incidence of brain metastasis, research on biomarkers for LUAD-BrM through proteomics of plasma EVs remains limited. This study represents the largest analysis of plasma EVs in LUAD to date, encompassing plasma samples from 217 participants. To address the significant challenges posed by LUAD-BrM and improve clinical outcomes, this study established a progressive five-step framework for screening and validating liquid biopsy biomarkers associated with LUAD-BrM. In Step 1, proteomic analysis of plasma EVs from 59 LUAD patients (30 BrM vs 29 non-BrM) identified 35 DEEPs. Functional enrichment analyses (GO, Reactome, GSEA) indicated a significant involvement of collagen-containing ECM and related pathways, which is consistent with previous reports in both tissue and plasma EV proteomic studies of LUAD/NSCLC brain metastasis [37, 38]. The ECM plays a dual role in metastasis: its fibrous structure provides scaffolding, tracks, and migration pathways that facilitate cancer cell dissemination, while its dense network can form a physical barrier that impedes cell migration [49]. The basement membrane of the blood–brain barrier (BBB) exemplifies a typical ECM structure, and its degradation may be essential for tumor cells to breach the BBB and establish metastatic lesions [50].

Steps 2 and 3 focused on target protein screening. Step 2 employed PPI network analysis to identify 16 candidate proteins, which showed significant enrichment in

collagen-containing ECM pathways. Three machine learning algorithms (LASSO, RF, SVM) further refined these to three hub proteins: LOX, FPR1, and ACTB. LOX mediates collagen/elastin cross-linking within the ECM, modulating tumor microenvironment remodeling, thus exerting either a promoting or inhibitory effect on tumor progression [39]. Given the central role of LOX in ECM protein cross-linking, its downregulation strongly aligns with the consistent downregulation of ECM-related pathways observed in both our study and previous reports [37, 38]. FPR1 induces chemotactic migration, epithelial-mesenchymal transition and angiogenesis in various malignancies [51]. ACTB, as a key cytoskeletal component, facilitates invasion and metastasis through the regulation of cell motility and matrix metalloproteinase secretion [52]. In Step 3, considering the organ heterogeneity associated with lung cancer metastasis [53], proteomic analysis of FFPE primary lung tumor tissues from 13 LUAD patients was performed. The results revealed a significant downregulation of LOXL1 in the BrM group. This analysis aimed to identify LUAD-BrM-specific risk proteins and to assess their correlation with findings from EV proteomics. UALCAN database analysis further indicated that the downregulation of the LOX family (LOX/LOXL1) was not a consistent event during general LUAD progression, supporting its specific association with the BrM phenotype. Although the three previously mentioned hub proteins were not directly identified, LOXL1, which shares structural and functional similarities with LOX [39, 54], was significantly downregulated in the BrM group, which was also validated through IHC. The results underscore the critical role of the LOX family in the progression of LUAD-BrM.

Steps 4 and 5 progressed from transcriptomic mapping to protein-level validation, employing ELISA and Western blot to establish the translational value of plasma EV-derived LOX as a LUAD-BrM risk-associated biomarker. In Step 4, we assessed the transcriptional profile of LOX using single-cell databases. At the single-cell level, LOX is primarily expressed in fibroblasts, which are key regulators of ECM homeostasis [55]. Notably, LOX expression was significantly downregulated in NSCLC-BrM datasets compared to in situ NSCLC, with fibroblasts exhibiting low LOX levels showing suppressed ECM assembly and remodeling pathways. Importantly, bioinformatic analysis further revealed that LOX-low fibroblasts were enriched for the PI3K/AKT signaling pathway, prompting us to investigate a potential regulatory axis. Although earlier studies suggested context-dependent roles for LOX in tumor progression [39, 54, 56], direct evidence linking LOX to BrM remains scarce. In our study, plasma EV-derived LOX was significantly decreased in BrM patients. To functionally probe this potential PI3K/AKT-LOX-ECM axis, we performed complementary in vitro experiments. We found that pharmacological inhibition of PI3K/AKT signaling rstored LOX expression in fibroblasts, positioning it as an upstream regulator. Conversely, direct inhibition of LOX activity led to decreased expression of key ECM components, including collagen and α-SMA, corroborating our histological observations in patient tissues. These functional data lend mechanistic support to the link between LOX downregulation and ECM degradation. In Step 5, we translated these findings to clinical validation. ELISA analysis of an independent validation cohort demonstrated that plasma EV-derived LOX showed superior ability to distinguish BrM, underscoring its liquid biopsy potential. Supporting Western blot analysis confirmed the consistent downregulation of LOX and LOXL1 in BrM patient tissues and plasma EVs. Collectively, evidence from transcriptomics, functional assays, and protein validation across cohorts converges to robustly associate LOX downregulation with LUAD-BrM. Therefore, we propose a model wherein activation of the PI3K/AKT pathway in the tumor microenvironment suppresses LOX expression in fibroblasts; the resultant LOX deficiency, carried by EVs, contributes to ECM destabilization and may facilitate BBB weakening, thereby promoting brain metastasis in LUAD.

This study utilized a homogeneous cohort of stage IV LUAD patients categorized by BrM status, minimizing disease heterogeneity and strengthening the association between protein expression and the BrM phenotype. The application of high-performance DIA-MS proteomics enhanced the detection reliability of low-abundance exosomal proteins, thus improving proteomic coverage and reproducibility. Our integrated multi-omics strategy converges multiple lines of evidence to support the role of LOX in LUAD-BrM: consistent downregulation of LOX/LOXL1 in tissues and plasma EVs; single-cell transcriptomics linking low LOX in fibroblasts to impaired ECM pathways; in vitro functional data suggesting a PI3K/AKT-LOX-ECM axis; and the confirmed downregulation and diagnostic power of plasma EV-derived LOX in an independent validation cohort. This strategy not only reinforces the biological relevance of LOX but also provides insights into its potential cellular origin (fibroblasts) and mechanistic pathway. By integrating the clinical value of exosomal biomarkers with their organotropism mechanisms, this study establishes plasma exosomal LOX as a promising non-invasive biomarker for LUAD-BrM and proposes a model for its role in brain-tropic metastasis. These findings may facilitate cost-effective early screening, enhance risk stratification, and enable timely intervention in high-risk patients, ultimately reducing BrM-related mortality. Undeniably, this study has certain limitations. The single-center design may introduce

selection bias despite the relatively large cohort of 260 patients. Additionally, the FFPE tissues were not sourced from the same patients providing plasma samples, which precludes direct correlation analysis between exosomal and tissue LOX expression. Third, while our integrated analysis robustly links LOX downregulation to the BrM phenotype, the study design is limited by the absence of normal lung tissue and sequential samples from the same individuals. Therefore, we cannot delineate the precise trajectory of LOX dysregulation from early LUAD to metastasis, nor definitively rule out its alteration as a more general tumor-associated event. This specifically precludes us from drawing definitive conclusions about the baseline expression of plasma EV-derived LOX relative to a healthy state. Finally, while our in vitro data suggest a PI3K/AKT-LOX-ECM axis, the mechanistic role of LOX in LUAD-BrM requires further in vivo elucidation. Future studies should incorporate longitudinal cohorts with matched normal-primary-metastatic samples, in vivo functional validation, multi-center prospective validation, and integrated omics approaches to establish its clinical utility.

Conclusions

This study identifies plasma exosomal LOX as a non-invasive biomarker associated with the risk of brain metastasis in lung adenocarcinoma through an integrated multi-omics strategy. Mechanistically, PI3K/AKT-mediated LOX downregulation contributes to brain metastasis by disrupting extracellular matrix integrity and impairing the blood–brain barrier. Public data confirm that LOX family downregulation is specifically associated with the brain metastasis phenotype rather than general tumor progression. Clinically, plasma exosomal LOX demonstrates favorable diagnostic performance compared to direct plasma detection. Our findings provide a potential liquid biopsy target for screening high-risk LUAD-BrM patients and offer new insights into organotropic metastasis mechanisms.

Abbreviations

BBB	Blood-brain barrier
BrM	Brain metastasis
DEEPs	Differentially expressed exosomal proteins
DIA-MS	Data-independent acquisition mass spectrometry
ECM	Extracellular matrix
ELISA	Enzyme-linked immunosorbent assay
EVs	Extracellular vesicles
FFPE	Formalin-fixed paraffin-embedded
GO	Gene Ontology
GSEA	Gene Set Enrichment Analysis
IHC	Immunohistochemistry
KEGG	Kyoto Encyclopedia of Genes and Genomes
LASSO	Least absolute shrinkage and selection operator
LOX	Lysyl oxidase
LOXL1	Lysyl Oxidase-Like 1
LUAD	Lung adenocarcinoma
LUAD-BrM	Lung adenocarcinoma with brain metastasis
non-BrM	None brain metastasis
NTA	Nanoparticle tracking analysis
PPI	Protein-protein interaction
RF	Random forest
SEC	Size exclusion chromatography
SVM	Support vector machine
TDEVs	Tumor-derived extracellular vesicles
TEM	Transmission electron microscopy

Supplementary Information

The online version contains supplementary material available at https://doi.org/10.1186/s12916-026-04785-0.

Additional file 1. Supplementary experimental details on proteomics and IHC, along with Fig. S1-S3. Fig. S1. Proteomic data correction and between/within-group differences. Fig. S2. Supplementary analysis of plasma-EV proteomic. Fig. S3. LOX/LOXL1 expression from UALCAN database

Additional file 2: Table S1-S4. Table S1. Characteristics of the LUAD patients. Table S2. Quantified values of each plasma EV protein after normalization. Table S3. Differentially expressed plasma EV proteins. Table S4. Differentially expressed proteins in FFPE tissues

Additional file 3. Original gel and blot images

Acknowledgements

We extend our sincere gratitude to Duolaimi Biotechnology (Wuhan) Co., Ltd. for their invaluable assistance in the proteomics research conducted during this study.

Authors' contributions

JL and WG were responsible for the conception, design, and project administration. JL, YP, and JLS performed the investigation, data curation, and wrote the original draft. JL and YP conducted the formal analysis. HXY, JZ, FH, and CTW provided sample resources. YP and YY contributed to visualization. YL and YY performed bioinformatics analysis. YL, XJH, and WG were responsible for the review and editing of the manuscript. JL and WG acquired funding. YL and YY provided supervision. All authors read and approved the final manuscript.

Funding

The study was supported by the Innovation and Development Joint Fund of Hubei Natural Science (No. 2025AFD098, 2024AFD427), Young Talents Development Program of Xiangyang Central Hospital (2025RCYC-034) and Research of Xiangyang Central Hospital Scientific Project (2024YJ04A).

Data availability

The mass spectrometry proteomics data have been deposited in the ProteomeXchange Consortium (https://proteomecentral.proteomexchange.org) via the iProX partner repository with the dataset identifier PXD068757.

Declarations

Ethics approval and consent to participate

This study was conducted in accordance with the ethical principles of the Declaration of Helsinki. This study was approved by the Ethics Committee of Xiangyang Central Hospital (Ethics Approval Number: 2021–054). The participants provided their written informed consent to participate in this study.

Consent for publication

Not applicable.

Competing interests

The authors declare no competing interests.

Author details
[1]Department of Oncology, Xiangyang Central Hospital, affiliated hospital of Hubei University of Arts and Science, Xiangyang 441021, China. [2]Institute of Oncology, Xiangyang Central Hospital, affiliated hospital of Hubei University of Arts and Science, Xiangyang 441021, China. [3]School of Pharmacy, Hubei University of Chinese Medicine, Wuhan 430065, China.

Received: 9 October 2025 Accepted: 5 March 2026
Published: 12 March 2026

References

1. Bray F, Laversanne M, Sung H, Ferlay J, Siegel RL, Soerjomataram I, et al. Global cancer statistics 2022: Globocan estimates of incidence and mortality worldwide for 36 cancers in 185 countries. CA Cancer J Clin. 2024;74:229–63.
2. Lah TT, Novak M, Breznik B. Brain malignancies: glioblastoma and brain metastases. Semin Cancer Biol. 2020;60:262–73.
3. Zuccato JA, Mamatjan Y, Nassiri F, Ajisebutu A, Liu JC, Muazzam A, et al. Prediction of brain metastasis development with DNA methylation signatures. Nat Med. 2024;31:116–25.
4. Lamba N, Wen PY, Aizer AA. Epidemiology of brain metastases and leptomeningeal disease. Neuro Oncol. 2021;23:1447–56.
5. Robinson SD, de Boisanger J, Pearl FMG, Critchley G, Rosenfelder N, Giamas G. A brain metastasis liquid biopsy: where are we now? Neuro-Oncol Adv. 2024;6:vdae066.
6. Dwarshuis G, Kroon LL, Brandsma D, Noske DP, Best MG, Sol N. Liquid biopsies for the monitoring of gliomas and brain metastases in adults. Acta Neuropathol. 2025;149:37.
7. Ignatiadis M, Sledge GW, Jeffrey SS. Liquid biopsy enters the clinic - implementation issues and future challenges. Nat Rev Clin Oncol. 2021;18:297–312.
8. Heitzer E, Haque IS, Roberts CES, Speicher MR. Current and future perspectives of liquid biopsies in genomics-driven oncology. Nat Rev Genet. 2018;20:71–88.
9. Rehman AU, Khan P, Maurya SK, Siddiqui JA, Santamaria-Barria JA, Batra SK, et al. Liquid biopsies to occult brain metastasis. Mol Cancer. 2022;21:113.
10. Zheng M-M, Zhou Q, Chen H-J, Jiang B-Y, Tang L-B, Jie G-L, et al. Cerebrospinal fluid circulating tumor DNA profiling for risk stratification and matched treatment of central nervous system metastases. Nat Med. 2025;31:1547–56.
11. Kalluri R, LeBleu VS. The biology, function, and biomedical applications of exosomes. Science. 2020;367:aau6977.
12. Yu D, Li YX, Wang MY, Gu JM, Xu WR, Cai H, et al. Exosomes as a new frontier of cancer liquid biopsy. Mol Cancer. 2022;21:56.
13. Zhou B, Xu K, Zheng X, Chen T, Wang J, Song Y, et al. Application of exosomes as liquid biopsy in clinical diagnosis. Signal Transduct Target Ther. 2020;5:144.
14. Kalluri R, McAndrews KM. The role of extracellular vesicles in cancer. Cell. 2023;186:1610–26.
15. Zhang C, Qin C, Dewanjee S, Bhattacharya H, Chakraborty P, Jha NK, et al. Tumor-derived small extracellular vesicles in cancer invasion and metastasis: molecular mechanisms, and clinical significance. Mol Cancer. 2024;23:18.
16. Jiang C, Zhang N, Hu X, Wang H. Tumor-associated exosomes promote lung cancer metastasis through multiple mechanisms. Mol Cancer. 2021;20:117.
17. Yin L, Liu X, Shao X, Feng T, Xu J, Wang Q, et al. The role of exosomes in lung cancer metastasis and clinical applications: an updated review. J Transl Med. 2021;19:312.
18. Urabe F, Patil K, Ramm GA, Ochiya T, Soekmadji C. Extracellular vesicles in the development of organ-specific metastasis. J Extracell Vesicles. 2021;10:e12125.
19. Syn N, Wang L, Sethi G, Thiery J-P, Goh B-C. Exosome-mediated metastasis: from epithelial-mesenchymal transition to escape from immunosurveillance. Trends Pharmacol Sci. 2016;37:606–17.
20. Oliveira FD, Castanho MARB, Neves V. Exosomes and brain metastases: a review on their role and potential applications. Int J Mol Sci. 2021;22:10899.
21. Hoshino A, Costa-Silva B, Shen T-L, Rodrigues G, Hashimoto A, Tesic Mark M, et al. Tumour exosome integrins determine organotropic metastasis. Nature. 2015;527:329–35.
22. Rodrigues G, Hoshino A, Kenific CM, Matei IR, Steiner L, Freitas D, et al. Tumour exosomal cemip protein promotes cancer cell colonization in brain metastasis. Nat Cell Biol. 2019;21:1403–12.
23. Simpson RJ, Kalra H, Mathivanan S. Exocarta as a resource for exosomal research. J Extracell Vesicles. 2012;1:18374.
24. Chitti SV, Gummadi S, Kang T, Shahi S, Marzan AL, Nedeva C, et al. Vesiclepedia 2024: an extracellular vesicles and extracellular particles repository. Nucleic Acids Res. 2024;52:D1694-d8.
25. Wang L, Dai J, Han R, Jin W. Single-cell map of diverse immune phenotypes in the metastatic brain tumor microenvironment of non small cell lung cancer and triple negative breast cancer. Gene Expression Omnibus. 2020. https://identifiers.org/geo/GSE143423.
26. Wang L, Chao M, Han RR, Li L, Dong L, Chen F, et al. Single-cell map of diverse immune phenotypes in the metastatic brain tumor microenvironment of nonsmall-cell lung cancer. Int J Surg. 2025;111:1601–6.
27. Chi Y, Remsik J, Kiseliovas V, Pe'er D, Mazutis L, Boire A. Single-cell atlas of human leptomeningeal metastasis. Gene Expression Omnibus. 2020. https://identifiers.org/geo/GSE150660.
28. Chi Y, Remsik J, Kiseliovas V, Derderian C, Sener U, Alghader M, et al. Cancer cells deploy lipocalin-2 to collect limiting iron in leptomeningeal metastasis. Science. 2020;369:276–82.
29. Zilionis R, Engblom C, Pfirschke C, Savova V, Zemmour D, Saatcioglu HD, et al. Single cell transcriptomics of human and mouse lung cancers reveals conserved myeloid populations across individuals and species. Gene Expression Omnibus. 2019. https://identifiers.org/geo/GSE127465.
30. Zilionis R, Engblom C, Pfirschke C, Savova V, Zemmour D, Saatcioglu HD, et al. Single-cell transcriptomics of human and mouse lung cancers reveals conserved myeloid populations across individuals and species. Immunity. 2019;50:1317-34.e10.
31. Fan J. Comprehensive Profiling of Cancer Cells and Their Microenvironment in Advanced NSCLC. Gene Expression Omnibus. 2021. https://identifiers.org/geo/GSE148071.
32. Wu F, Fan J, He Y, Xiong A, Yu J, Li Y, et al. Single-cell profiling of tumor heterogeneity and the microenvironment in advanced non-small cell lung cancer. Nat Commun. 2021;12:2540.
33. Han Y, Wang Y, Dong X, Sun D, Liu Z, Yue J, et al. Tisch2: Expanded datasets and new tools for single-cell transcriptome analyses of the tumor microenvironment. Nucleic Acids Res. 2023;51:D1425–31.
34. Hänzelmann S, Castelo R, Guinney J. Gsva: gene set variation analysis for microarray and rna-seq data. BMC Bioinformatics. 2013;14:7.
35. Schubert M, Klinger B, Klünemann M, Sieber A, Uhlitz F, Sauer S, et al. Perturbation-response genes reveal signaling footprints in cancer gene expression. Nat Commun. 2018;9:20.
36. Chandrashekar DSKS, Korla PK, Patel H, Shovon AR, Athar M, Netto GJ, et al. Ualcan: an update to the integrated cancer data analysis platform. Neoplasia. 2022;25:18–27.
37. Li S, Qu Y, Liu L, Zhang X, He Y, Wang C, et al. Comparative proteomic profiling of plasma exosomes in lung cancer cases of liver and brain metastasis. Cell Biosci. 2023;13:180.
38. Woldmar N, Schwendenwein A, Kuras M, Szeitz B, Boettiger K, Tisza A, et al. Proteomic analysis of brain metastatic lung adenocarcinoma reveals intertumoral heterogeneity and specific alterations associated with the timing of brain metastases. ESMO Open. 2023;8:100741.
39. Barker HE, Cox TR, Erler JT. The rationale for targeting the lox family in cancer. Nat Rev Cancer. 2012;12:540–52.
40. The Clinical Proteomic Tumor Analysis Consortium (CPTAC). CPTAC LUAD Discovery Study - Proteome. Proteomic Data Commons. 2021. https://pdc.cancer.gov/pdc/study/PDC000153.
41. Gillette MA, Satpathy S, Cao S, Dhanasekaran SM, Vasaikar SV, Krug K, et al. Proteogenomic characterization reveals therapeutic vulnerabilities in lung adenocarcinoma. Cell. 2020;182:200-25.e35.
42. The APOLLO Research Network. APOLLO LUAD - Proteome. Proteomic Data Commons. 2021. https://pdc.cancer.gov/pdc/study/PDC000434.
43. Soltis AR, Bateman NW, Liu J, Nguyen T, Franks TJ, Zhang X, et al. Proteogenomic analysis of lung adenocarcinoma reveals tumor heterogeneity, survival determinants, and therapeutically relevant pathways. Cell Rep Med. 2022;3:100819.

44. Zhao Y, Gu S, Li L, Zhao R, Xie S, Zhang J, et al. A novel risk signature for predicting brain metastasis in patients with lung adenocarcinoma. Neuro Oncol. 2023;25:2207–20.
45. Wang Z, Wang Y, Chang M, Wang Y, Liu P, Wu J, et al. Single-cell transcriptomic analyses provide insights into the cellular origins and drivers of brain metastasis from lung adenocarcinoma. Neuro Oncol. 2023;25:1262–74.
46. Tagore S, Caprio L, Amin AD, Bestak K, Luthria K, D'Souza E, et al. Single-cell and spatial genomic landscape of non-small cell lung cancer brain metastases. Nat Med. 2025;31:1351–63.
47. Duan H, Ren J, Wei S, Yang Z, Li C, Wang Z, et al. Integrated analyses of multi-omic data derived from paired primary lung cancer and brain metastasis reveal the metabolic vulnerability as a novel therapeutic target. Genome Med. 2024;16:138.
48. Xu Z-H, Miao Z-W, Jiang Q-Z, Gan D-X, Wei X-G, Xue X-Z, et al. Brain microvascular endothelial cell exosome-mediated s100a16 up-regulation confers small-cell lung cancer cell survival in brain. FASEB J. 2019;33:1742–57.
49. Eble JA, Niland S. The extracellular matrix in tumor progression and metastasis. Clin Exp Metastasis. 2019;36:171–98.
50. McDonald B, Barth K, Schmidt MHH. The origin of brain malignancies at the blood–brain barrier. Cell Mol Life Sci. 2023;80:282.
51. Prevete N, Liotti F, Marone G, Melillo RM, de Paulis A. Formyl peptide receptors at the interface of inflammation, angiogenesis and tumor growth. Pharmacol Res. 2015;102:184–91.
52. Guo C, Liu S, Wang J, Sun M-Z, Greenaway FT. ACTB in cancer. Clin Chim Acta. 2013;417:39–44.
53. Wood SL, Pernemalm M, Crosbie PA, Whetton AD. The role of the tumor-microenvironment in lung cancer-metastasis and its relationship to potential therapeutic targets. Cancer Treat Rev. 2014;40:558–66.
54. Ye MM, Song YZ, Pan SY, Chu M, Wang ZW, Zhu XQ. Evolving roles of lysyl oxidase family in tumorigenesis and cancer therapy. Pharmacol Ther. 2020;215:107633.
55. Liu Y, Zhang X, Gu W, Su H, Wang X, Wang X, et al. Unlocking the crucial role of cancer-associated fibroblasts in tumor metastasis: mechanisms and therapeutic prospects. J Adv Res. 2025;71:399–413.
56. Kenyon K, Contente S, Trackman PC, Tang J, Kagan HM, Friedman RM. Lysyl oxidase and rrg messenger rna. Science. 1991;253:802.

Publisher's Note